Graphene quantum dots sensitized In$_2$S$_3$ nanohybrids for improved photocatalytic activity

Yao Yao[1],* , Zhen Zhao[1], Huina Cui[1], Wenbin Dong[1], Zhengfeng Li[1], and Gangli Liao[1]

[1] *Ningxia Key Laboratory of Green Catalytic Materials and Technology, College of Chemistry and Chemical Engineering, Ningxia Normal University, Guyuan 756000, People's Republic of China*

ABSTRACT

A graphene quantum dots (GQDs) sensitized In$_2$S$_3$ heterostructure photocatalyst was synthesized via a one-pot hydrothermal synthesis route. The high-resolution transmission electron microscope (HR-TEM) images reveal that the In$_2$S$_3$/GQD adopts the self-assembly three-dimensional flower-like nanostructure, in which In$_2$S$_3$ forms the petal-like framework and the GQDs are grown on the surface of In$_2$S$_3$. The GQD has very high crystallinity and the loading amount of GQDs can be controlled during the synthesis process. The In$_2$S$_3$/GQDs catalyst exhibits extremely high adsorption capacity, photocatalytic activity and selectivity towards methylene blue. Under the identical experimental conditions, an optimum GQDs content of 1.09 wt% in the In$_2$S$_3$/GQDs nanocomposite resulted in 4.9 times higher dark adsorption rate and 3.7 times higher photodegradation rate for MB than pristine In$_2$S$_3$, making the In$_2$S$_3$/GQD a potential photocatalyst in water purification.

1 Introduction

The increasing global crisis of energy shortage and environmental issues are becoming serious threats to the further development of modern society [1]. Photocatalytic degradation of organic pollutants represents a promising strategy for the direct utilization of solar energy to address the increasing environmental and water resource concerns [2]. The photodegradation process basically involves three key aspects, (i) the effective utilization of solar energy, (ii) the generation and separation of photoexcited charge carriers, and (iii) the rapid surface catalytic reactions [1, 3].

Therefore, since the first report on TiO$_2$ photocatalyst in 1972 [4], many efforts have been made to improve the photocatalytic efficiency of semiconductors in accordance with these three priorities.

Recent years, the rapid development of indium-based photocatalysts, such as indium oxide (In$_2$O$_3$) and indium sulfide (In$_2$S$_3$), have witnessed the more efficient sensitization for extending the light absorption spectra from the UV into the visible light region [5]. As a typical example, In$_2$S$_3$ has been widely recognized as a promising candidate for broadband spectrum photocatalysis, showing the narrower band gap of 2.10 eV [6], unique electronic structures, high conductivity [7],

---

Yao Yao and Zhen Zhao have contributed equally to this work.

Address correspondence to E-mail: yaoyao_zz308@163.com

Ⓐ Springer

outstanding stability [8], non-toxicity [9], and also the well-positioned potentials of redox reaction. However, the high recombination and transfer kinetics of photo-excited charge carriers limit the photocatalytic performance of In_2S_3. Thus, several modification approaches have been reported in the literature. One promising approach to enhance the photocatalytic activity of In_2S_3 is to construct heterojunctions that facilitate photo-excited charge carrier separation. Such as to decorate In_2S_3 with noble metal or carbon nanomaterials [2, 10, 11], or construct heterojunction with another semiconductor to form a suitable band-alignment heterostructure.

Inspired by the above development, the modification of In_2S_3 with graphene quantum dots seem to be a good choice. Graphene quantum dots (GQDs), with the diameter less than 10 nm, have been demonstrated to be an effective surface photosensitizer to substantially improving the light absorption ability of semiconductor photocatalysts [12–14]. When irradiation occurs, the GQD acts as an electron acceptor or mediator to accelerate the photogenerated electron-hole pairs migration effectively [2, 12]. And the quantum effect of GQDs also endow enhanced optical properties for the hybrid catalyst [15, 16].

Herein, we report the facile one-pot hydrothermal synthesis of a In_2S_3/GQDs heterojunction. The as-obtained sample possessed a three-dimensional petal-like nanostructure with the GQDs appended on In_2S_3 surface. The interfaces between GQDs and In_2S_3 are relatively large and well bonded, thus resulting a significantly enhanced efficiency for photogenerated charge separation and transport [17]. As expected, the GQDs decorated In_2S_3 hybrids exhibited significantly enhanced photocatalytic activity toward methylene blue (MB) under simulate sun light irradiation compared with that of pristine In_2S_3. Furthermore, the underlying photocatalytic mechanism and the role of GQD were also investigated.

2 Experimental section

2.1 Materials

$InCl_3·4H_2O$ and thioacetamide (CH_3CSNH_2, TAA) were purchased from Aladdin Chemistry Co., Ltd. (Shanghai, China). Glucose and absolute ethanol were obtained from Sinopharm Chemical Reagent Co. Ltd.

(Shanghai, China). Distilled water was used in the experiments unless otherwise specifically stated.

2.2 Preparation

The In_2S_3/GQDs nanocomposite was synthesized by one-pot hydrothermal approach, just as Fig. 1a illustrated. In brief, $InCl_3·4H_2O$ (0.2345 g) and TAA (0.1050 g) were dissolved in 10 mL distilled water to form a clarified aqueous solution. Then, the appropriate amount of glucose was added in, after actively stirring for 10 min, transferred the above homogeneous solution into a 25 mL Teflon-sealed autoclave, heated to 180 °C and maintained for 12 h. After cooling down to room temperature naturally, the solid sample was centrifugation, washed with deionized water and ethanol for several times, and eventually dried at 60 °C for 5 h.

GQDs were obtained using an emulsion polymerization reaction of glucose under the hydrothermal condition during the one-pot synthesis process, therefore, the mass ratio of In_2S_3/GQDs can be controlled by adjusting the addition amount of glucose, and the corresponding obtained solid sample with the ID referenced by formula In_2S_3/GQDs-1 (glucose 0.0252 g), In_2S_3/GQDs-2 (glucose 0.0126 g), and In_2S_3/GQDs-3 (glucose 0.0072 g); for details, see Supporting Information, Table S1. And for the sake of comparison, pure In_2S_3 was also synthesized under the same preparation procedure without the addition of glucose.

2.3 Characterization

XRD was performed on X' Pert PRO (Panalytical Ltd.) with Cu Kα radiation diffractometer (k = 0.15406 nm) in 2θ range of 20–80°. SEM images were taken with a ZEISS Gemini 300. TEM was taken by a JEM-2100 F JEOL with the accelerating voltage of 200 kV, and with an attachment of EDX. XPS were collected with an AXIS ULTRA XPS instrument (Kratos Analytical Ltd.) with a monochromatic X-ray source of Al Kα. UV–Vis–NIR optical absorption spectra on the powders were measured using a Lambd1050 spectrometer (PerkinElmer Ltd.).

2.4 Photocatalytic performance measurements

The photocatalytic activity was evaluated by the degradation of methylene blue (MB) in aqueous solution, with the concertation of 30 mg/L. The In_2S_3/GQDs

Fig. 1 **a** A schematic illustration of synthesis procedure for the In$_2$S$_3$/GQDs, **b** XRD patterns and **c** Raman spectra of as-prepared samples
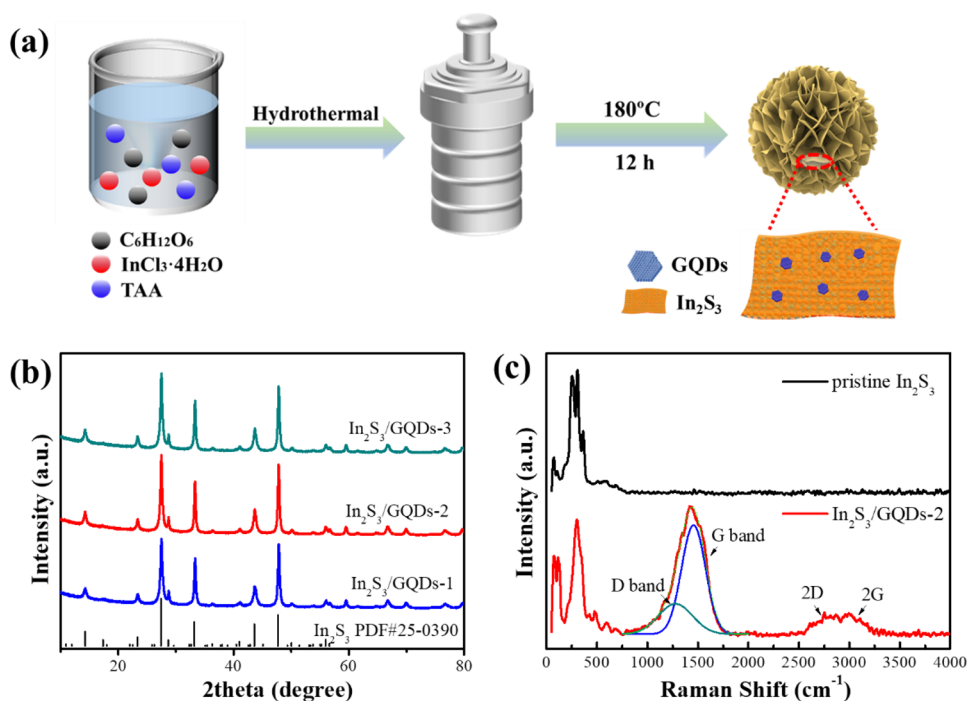

samples and pristine In$_2$S$_3$ (30 mg) were settled in 20 mL MB solution respectively, under the irradiation of a 300 W xenon arc light source (Microenerg Beijing Tech Co., Ltd., China), with the wavelength range of 300–2500 nm. The Cary 3500 UV–Vis spectrometer (Agilent Tech Co., Ltd.) was adopted to assess the photodegradation activity of the photocatalysts, and the photocatalytic degradation percentage can be calculated by the formula: D = C/C$_0$ × 100%, in which C$_0$ is the absorbency of the MB solution before illumination while C after it.

3 Results and discussion

The crystalline structure of as-prepared samples was investigated using X-Ray powder diffraction (XRD). The XRD pattern of GQDs shows a weak broad peak centered around 2θ = 24° (ESI Fig. S2), agrees well with the literature reported [18]. However, in the Fig. 1b, the as-prepared In$_2$S$_3$/GQDs composites only show the diffraction peaks of In$_2$S$_3$, tetragonal with the space group of l41/*amd* (141) (JCPDS card no. 25-0390). The introduction of GQDs does not leave obvious XRD signatures, suggesting that the loading amount of graphene quantum dots are getting too small, which is buried under the intense In$_2$S$_3$ diffraction [15, 19].

The existence of GQDs can be examined by surface-enhanced Raman scattering, using a 532 nm excitation, as shown in Fig. 1c. The characteristic peaks representing breathing and stretching vibration of sp^2 carbon are presented in the high frequency region [16]. The D and G band was around at ca.1500 cm^{-1}, and the peak at 2900 cm^{-1} can be assigned to 2D and 2G. Moreover, compared with the pristine In$_2$S$_3$ sample, the intensity of E^1_g and E^2_g vibration mode of In$_2$S$_3$ at low frequency region (75 and 115 cm^{-1}) was significantly enhanced by as much as 2.2 times in In$_2$S$_3$/GQDs [20], as explained by the quantum effect of graphene quantum dots [2].

The morphology and nanostructure of as-prepared sample are investigated by FE-SEM, TEM and HR-TEM. The low- and high-magnification FE-SEM images (Fig. 2a and b) of In$_2$S$_3$/GQDs-2 show that, large number of In$_2$S$_3$ nanosheets interweave with each other to construct a three-dimensional flower-like nanostructure, with the average size of ~ 5 μm. The In$_2$S$_3$ nanosheets seem to be structurally robust and ultra-thin (Fig. 2c), decorated by numerous GQDs, about ca. 3 nm in diameter (Fig. 2d and e). HR-TEM image shows a perfectly crystallized nanostructure of In$_2$S$_3$/GQDs-2, the detailed distribution of crystal planes as shown in Fig. 2f. The lattice fringes of a representative area show the spacing of ca. 0.23 nm, well in line with the crystallographic (1120) spacing of graphene quantum dots [21–23]. And we also noticed
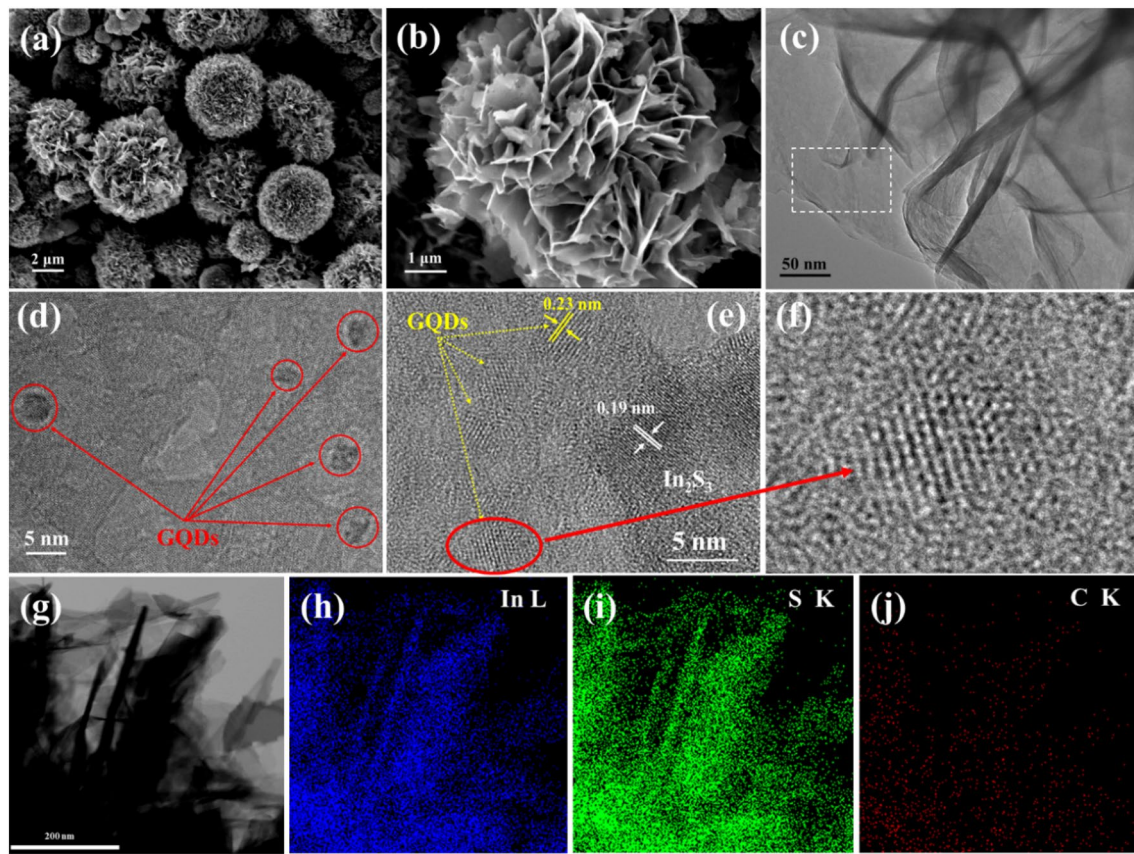
Fig. 2 **a** Low- and **b** high-magnification FE-SEM images of In$_2$S$_3$/GQDs-2. **c** TEM image of In$_2$S$_3$/GQDs-2. **d**, **e** and **f** HR-TEM image of a representative area. **g**–**j** EDX elemental mapping with respect to In, S and C elements

that another area shows the lattice fringe spacing of ca. 0.19 nm, which can be assigned to In$_2$S$_3$ (440) crystal plane (Fig. 2e). Innumerable graphene quantum dots are uniformly anchored on the In$_2$S$_3$ nanosheets and distributed in the entire nanoflower, forming a In$_2$S$_3$/GQDs hybrid nanostructure, as shown in the EDX elemental mapping results with respect to In, S and C elements (Fig. 2g–j).

The chemical composition and bonding states of In$_2$S$_3$/GQDs-2 are reconfirmed by X-ray photoelectron spectroscopy (XPS), as shown in Fig. 3. The survey-scan spectrum demonstrates that the as-prepared sample consists mainly of In, S and C elements (Fig. 3a), highly consistent with the EDX elemental mapping results. Therein, two sharp peaks at 445.1 and 452.6 eV, representing signatures of In 3d$_{5/2}$ and 3d$_{3/2}$ orbits of In$_2$S$_3$ (Fig. 3b). Figure 3c presents a high-resolution asymmetric S 2p XPS spectrum. After the curve fitting with a mixture function of Lorentzian and Gaussian, the S 2p peak can be deconvoluted

into two sub-peaks at 161.7 and 162.9 eV, representing signatures of S 2p$_{3/2}$ and S 2p$_{1/2}$ [16]. Likewise, the deconvolution of C 1s core-level spectrum shows three obviously sub-peaks located at 284.8, 285.4 and 286.7 eV (Fig. 3d), representing signatures of C–C (sp^2), C–C (sp) and C–S, respectively [16]. The area ratio of sp^2/sp is 2.5, implies that most of the C atoms in GQDs are arranged in a conjugated honeycomb lattice (sp^2 structure) [23]. Moreover, the high area ratio of In/S (8.10) and the presence of C–S sub-peak, indicating that the S atoms may dope into the graphene quantum dot matrix, and it is believed that the S ions substitution could facilitate partly C–C (sp) of carbon convert into C–C (sp^2) during the solvothermal synthetic process [16].

In order to investigate the interaction between photocatalyst and irradiation light, thereby the UV–Vis diffuse reflectance spectroscopy (DRS) of all samples was conducted, as shown in Fig. 4a. Their optical band gap energies can be calculated from the empirical equation:

Fig. 3 Typical XPS spectra of In$_2$S$_3$/GQDs-2 sample **a** in a wide survey scan, **b** in 3d region, **c** S 2p region and **d** C 1s region
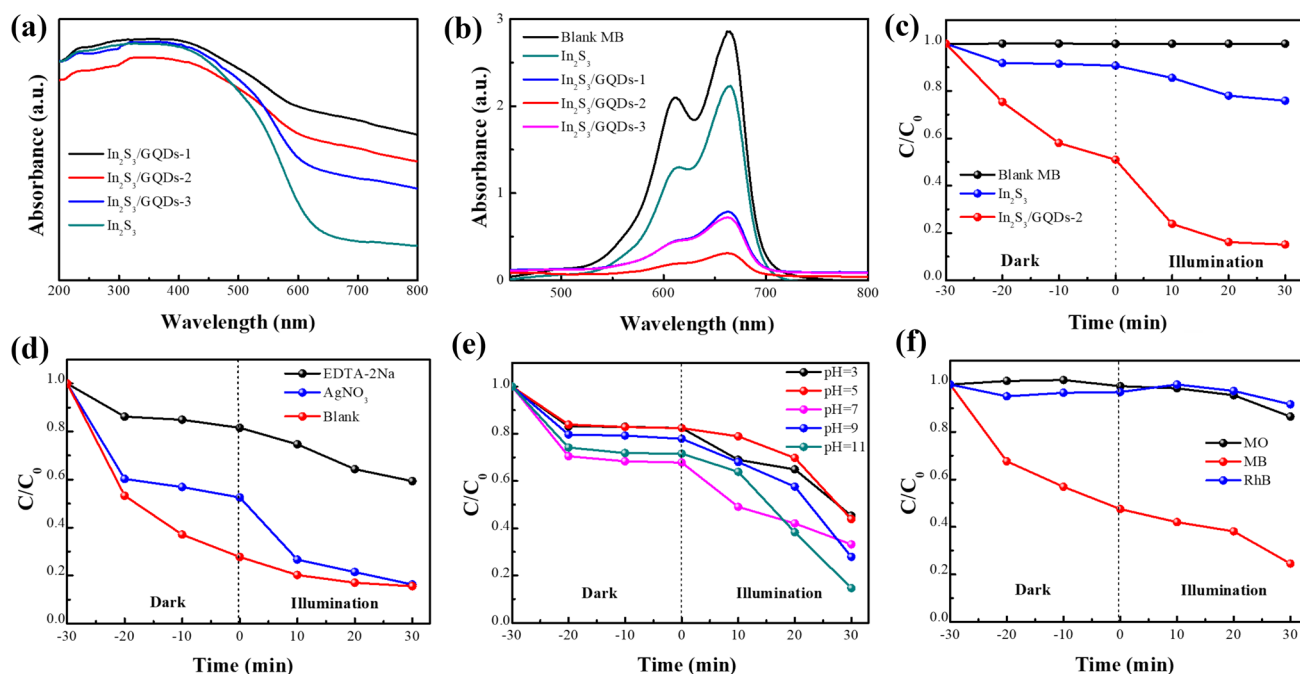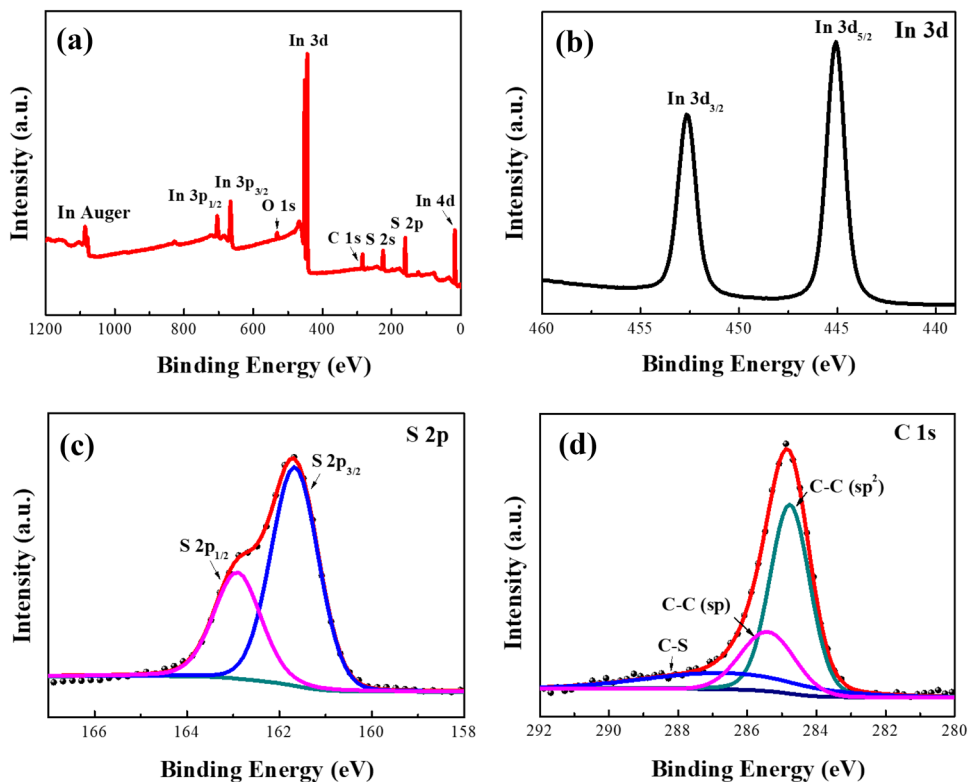
Fig. 4 **a** DRS spectra of the as-prepared samples. Photodegradation of MB solution **b** UV–Vis absorbance, **c** C/C$_0$ curve. Influence of operating parameters on the removal of MB and corresponding kinetic curves: **d** quenchers; **e** pH; and **f** selectivity of In$_2$S$_3$/GQDs-2 catalyst

$$Ahv = A\left(hv - E_g\right)^n, \tag{1}$$

where E_g is the optical band gap energy, v is the frequency of light, h is Planck's constant, n is equal to 1/2 for an allowed direct transition and constant A is define [24]. The pristine In_2S_3 shows the intrinsic absorption starting at 620 nm, corresponding to a band gap of 2.08 eV (ESI Fig. S3). Compared with that, all the composite samples exhibit the significant enhancement of light adsorption in the visible and near-infrared light region. The adsorption intensities are compatible with the addition amount of carbon, suggesting that graphene quantum dots are very beneficial for the broadband spectrum photocatalyst sensitization and light harvesting [25]. There is a not-so-obvious small peak at ca. 300 nm, attributed to the $\pi-\pi^*$ transition of aromatic sp^2 adsorption due to the GQDs [25–27]. Meanwhile, the red-shift of optical absorption in In_2S_3/GQDs samples are also observed. The band gap of In_2S_3/GQDs-2 was reduced to 1.8 eV, smaller than that of In_2S_3/GQDs-1 (1.83 eV), In_2S_3/GQDs-3 (1.97 eV) and pure In_2S_3 (2.08 eV) (ESI Fig. S3). Considering that the In_2S_3/GQDs samples have the same chemical composition, therefore the key point for such improvement depends on the loading amount of GQDs on the In_2S_3 surface [28].

In order to evaluate and verify whether the loading capacity of graphene quantum dot on the surface of In_2S_3 can enhance the light harvesting ability and photocatalytic performance, the photodegradation test of as-prepared samples under simulate sunlight was preformed, using methylene blue (MB) as the target, as shown in Fig. 4b and ESI Fig. S5. Apparently, under the same experimental condition, the photocatalyst In_2S_3/GQDs-2 shows the highest photo-decomposition rate of 90% after 30 min irradiation, while the pure In_2S_3, In_2S_3/GQDs-1 and In_2S_3/GQDs-3 only show the ratios of 24, 72 and 75%, respectively. The corresponding plots of MB concentration *versus* irradiation time with different samples are shown in Fig. 4c and ESI Table S2. Obviously, the sample In_2S_3/GQDs-2 has the highest photodegradation ratio towards MB with the GQDs loading amount of 1.09 wt%. However, on further whether increasing the loading amount of GQDs to 2.31 wt% (In_2S_3/GQDs-3), or decreasing to 0.63 wt% (In_2S_3/GQDs-1), the photodegradation rate of MB both decreased. This result suggested that the loading amount of GQDs may play a key role in photocatalysis progress (ESI Fig. S5). The surplus GQDs may prevent the photogenerated carriers from reacting with the chemisorbed oxygen to produce active radicals (e.g., $\cdot O_2$, $\cdot OH$) [29].

In order to investigate the underlying photocatalytic mechanism, EDTA-2Na and $AgNO_3$ were used as the scavengers for h^+ and e^-, respectively. As indicated, a negligible change in MB degradation was observed by adding $AgNO_3$ quencher (Fig. 4d), demonstrating that reactive oxygen species ($\cdot O^-_2$) was not the key point during the photodegradation reaction process [30]. By contrast, the photodegradation rate was significantly decreased from 84 to 40% after EDTA-2Na added in (ESI Table S3), indicating that the h^+ was responsible for the dye photodegradation [31].

Meanwhile, the surface discharge and photo-induced radical species of catalyst are also affected by the pH value [32]. It's reported that the high pH was more suitable for the formation of $\cdot OH$ radical via the reaction between OH^- and h^+ [32, 33]. Thus, the photocatalytic activity of In_2S_3/GQDs-2 increased from 55 to 85% with the elevating pH, as shown in Fig. 4e and ESI Table S4. This result highlights the strong influence of $\cdot OH$ radical on In_2S_3/GQDs-2 toward the MB photodegradation, indicating that the h^+ is indeed the key point during the photocatalytic process, well in line with the Fig. 4d result.

This conclusion also can be evidenced by the selectivity experiment towards different dyes, as shown in Fig. 4f. It is clear that the In_2S_3/GQDs-2 photocatalyst exhibits the highest photodegradation ratio of 75.5% towards MB, while it shows only minimal activities to other dyes including MO and Rh B (13.6 and 8.4%) under the same test concentration, demonstrating that the In_2S_3/GQDs-2 catalyst has remarkably good selectivity to MB. As we know, the structure of organic dye plays a crucial role during the catalytic process [34]. It is believed that the underlying mechanism is that the MB has an inclined conformation that permits easier access of $C-S^+=C$ groups to the catalyst surface [34], which is then dissociated by the hydroxyl radical ($\cdot OH$), eventually leading to the formation of sulfate ions [35].

The photogenerated charge carriers' behavior of In_2S_3/GQD-2 catalyst was also evaluated, compared with the pristine In_2S_3 sample, as shown in Fig. 5. The photocurrent density of In_2S_3/GQD-2 is much higher than that of pristine In_2S_3, which revealing the better charge transfer and separation rate in In_2S_3/GQD-2 (Fig. 5a) [36, 37]. Meanwhile, the electrochemical impedance spectroscopy (EIS) measurement was also
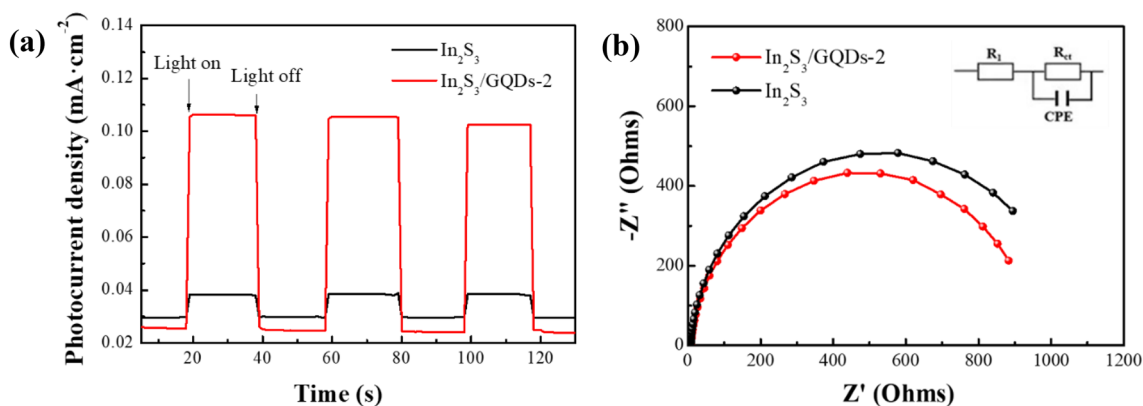
Fig. 5 a Transient photocurrent response and **b** Nyquist plots of pristine In_2S_3 and In_2S_3/GQDs-2 catalyst

carried out at 0.45 V (vs. RHE). Figure 5b shows the Nyquist plots of the samples, fitted using an equivalent Randles circuit with charge transfer resistance (R_{ct}). The In_2S_3/GQD-2 catalyst exhibits an R_{ct} of 900 Ω, much smaller than that of pure In_2S_3 (1200 Ω).

In_2S_3/GQD provides a promising approach for the conversion of organic wastes to CO_2 and H_2O. As we know, the MB molecule consists of several types of chemical bonds, such as aromatic rings, $C-S^+=C$, $C-N^+=C$, etc [38]. For the purpose of studying reaction process of photocatalysis, the FT-IR was used to investigate the photodegradation mechanisms, as shown in Fig. 6a. Exposure of MB-In_2S_3/GQDs suspension to xenon lamp illumination caused the rapid decay of MB molecule. After 30 min irradiation, the discernible bands emerged were isolated N–H stretching vibration at 3447 cm^{-1}, C–H stretching and bending vibration at 2921 and 1382 cm^{-1}, $-NO_2$ stretching vibration at 1593 and 1323 cm^{-1}, and S–O of sulfate ion (SO_4^{2-}) at 1228 cm^{-1}, suggesting that the elements such as S and N in methylene blue are typically oxidized into NH_4^+/NO_3^-, SO_4^{2-} and other small inorganic molecules [38], adsorbed on the In_2S_3/GQDs catalyst surface. This view was further evidenced by the LC–MS, as shown in Fig. 6b. The blue MB solution shows the rapid decay under irradiation (inset of Fig. 6b). After 60 min illumination, all the peaks intensity sharply decreased compared with the MB solution before irradiation, suggesting that the dye molecule was fully destructed by the In_2S_3/GQD-2 photocatalyst [39].

The stability is also very important for the photocatalyst, therefore, the cycling stability test was conducted in a continuous measurement mode, as shown in the Fig. 6c. The photocatalyst was

conducted for 5 consecutive test cycles, with 50 min for each cycle. The results show that the photodegradation efficiency of In_2S_3/GQD-2 catalyst slightly decreased from 97.3 to 91.6% after 5 times continuous cyclic test, indicating that In_2S_3/GQD-2 has remarkable reproducibility and excellent long-term stability [40, 41].

In order to further verify the stability of catalyst, the morphology and crystalline phase of In_2S_3/GQD-2 after circular experiment were characterized, as shown in Fig. S4. Compared with the catalyst before photodegradation (Figs. 1b and 2a), the morphology of In_2S_3/GQD-2 shows no obvious change (Fig. S4a). The new diffraction peak appears at $2\theta = 27.5, 33.3$ and $43.7°$ can be assigned to residual methylene blue hydrate [40, 42] (Fig. S4b).

The photocatalytic degradation of methylene blue involves two steps: (i) the generation of photoexcited charge carriers (i.e., electron and hole) under illumination, and (ii) the charge carriers react with chemisorbed oxygen and adsorbed reactants to initiate a series of bond-breaking and redox reaction, eventually leading to the formation of CO_2, H_2O, and other small inorganic molecules [38, 43, 44], as shown in Fig. 7a.

In_2S_3 and GQDs in the catalyst show the perfect interfacial contact, thus resulting in a heterojunction barrier for the transport of photon-generated carriers [45]. Considering the work function of GQDs (4.42 eV) [45, 46] is smaller than the In_2S_3 (4.55 eV) [47], thus, the transfer of electrons from the conduction band of In_2S_3 to GQDs is favorable. The valence band (VB) potentials (1.30 eV) and the conduction band (CB) potential (− 0.78 eV) of In_2S_3 can be calculated by the Eqs. (2) and (3) as following:
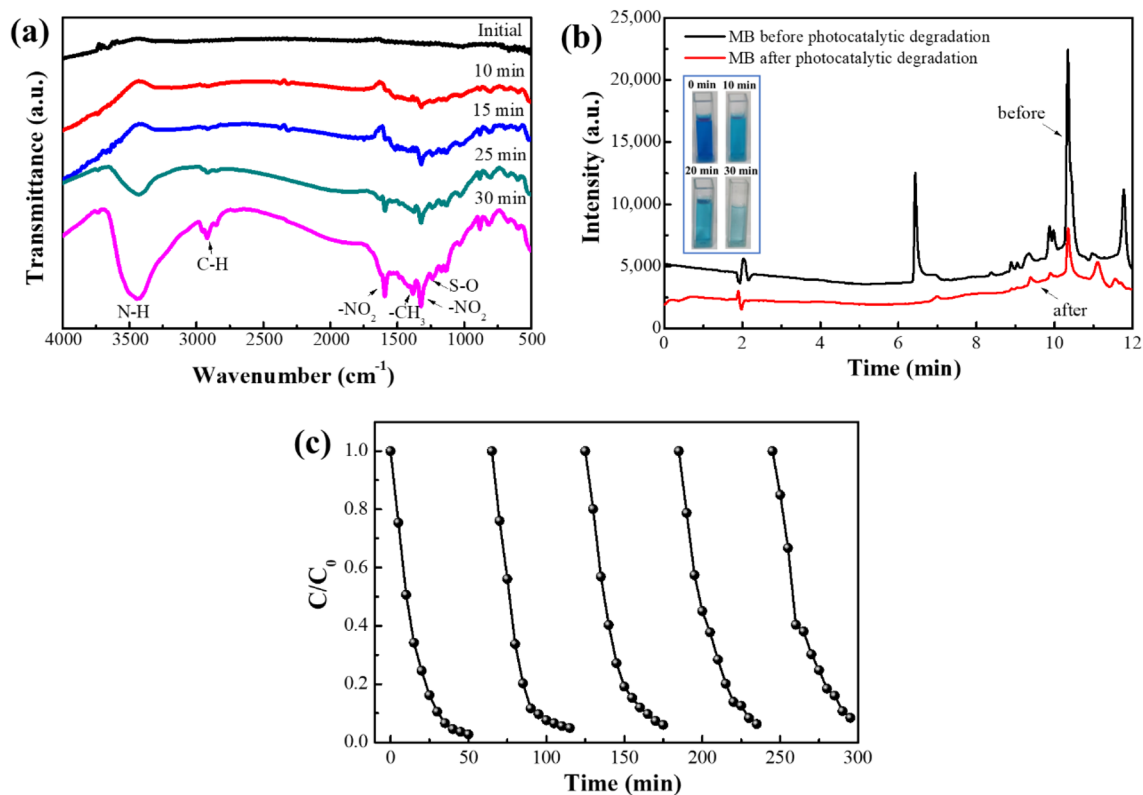
Fig. 6 a FT-IR spectra of In₂S₃/GQDs-2 as a function of reaction time; **b** LC–MS profile of Methylene Blue dye before and after photocatalytic degradation; (Inset: Photographs of In₂S₃/ GQDs-2 photodegrade MB at different times). **c** Photocatalyst stability tests of In₂S₃/GQDs-2 catalyst

Fig. 7 Photocatalytic mechanism of **a** a schematic diagram and **b** the charge transfer of In₂S₃/GQDs under irradiation
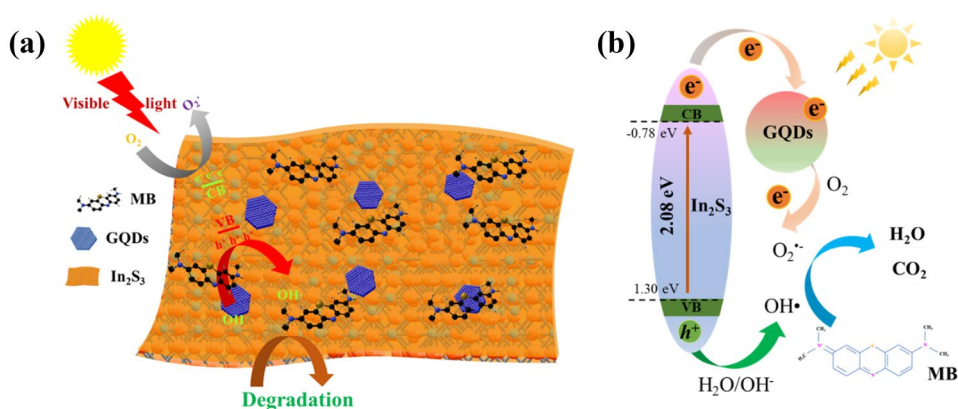
$$E_{VB} = X - E^C + 0.5E_{g'} \qquad (2)$$

$$E_{CB} = E_{VB} - E_{g'} \qquad (3)$$

where the X represents electro-negativity of the semiconductor material, the values of which for pure In₂S₃

is 4.76 eV, and E^c is the energy of free electrons on the hydrogen scale (ca. 4.5 eV) [24].

Herein, GQD exists as a blocking area, which can trap electrons emitted from the conduction band of In₂S₃ layer, resulting in a lower e⁻/h⁺ recombination rate [15, 48]. Meanwhile, the photogenerated holes left in the

valence band of In_2S_3 will migrate to the surface of catalyst, react with the adsorbed reactants for the oxidation reactions [12, 49, 50] (Fig. 7b). Therefore, the combination of In_2S_3 and GQDs not only can promote the light harvesting by extending the light absorption region, but also can facilitate the charge-carrier separation [2, 12, 45, 48], thereby yielding an improved photocatalytic efficiency.

4 Conclusion

In conclusion, a facile one-pot hydrothermal method was employed to synthesize In_2S_3/GQDs heterostructure with excellent adsorption and photocatalytic performance in the full-spectrum light range. The graphene quantum dot can be applied as a photosensitizer and mediator for improving the light-harvesting capacity of In_2S_3. For comparison to pure In_2S_3, the synergistic effect between GQDs and In_2S_3 generally enhanced the adsorption-photocatalytic ability of In_2S_3/GQDs nanocomposites. It's ascribed to the large specific surface area, abundant active sites formed at the junction interfaced and also the better photo-excited charge carrier separation, finally resulting in improved photocatalytic activity.

Author contributions

YY: Conceptualization, Formal Analysis, Funding Acquisition, Resources, Supervision, Writing—Original Draft, Review & Editing. ZZ: Methodology, Investigation, Data Curation, Formal Analysis, Validation. HC: Validation. WD: Investigation. GL: Software. ZL: Additional experiments.

Funding

Data availability

All data generated or analysed during this study are included in this published article [and its supplementary information files].

Declarations

Competing interest　The authors declare no competing financial interests.

Supplementary Information　The online version contains supplementary material available at https://doi.org/10.1007/s10854-023-11399-2.

References

1. S. Cao, J. Low, J. Yu, M. Jaroniec, Adv. Mater. **27**, 2150 (2015). https://doi.org/10.1002/adma.201500033
2. H. Zhang, L. Zhao, F. Geng, L.-H. Guo, B. Wan, Y. Yang, Appl. Catal. B **180**, 656 (2016). https://doi.org/10.1016/j.apcatb.2015.06.056
3. J. Liu, J. Ke, D. Li et al., ACS Appl. Mater. Interfaces **9**, 11678 (2017). https://doi.org/10.1021/acsami.7b01605
4. A. Fujishima, K. Honda, Nature **238**, 37 (1972). https://doi.org/10.1038/238037a0
5. X. Chen, W. Zhang, L. Zhang et al., ACS Appl. Mater. Interfaces **13**, 25868 (2021). https://doi.org/10.1021/acsami.1c02953
6. S. Zhao, K. Li, J. Du, C. Song, X. Guo, ACS Sustain. Chem. Eng. **9**, 5942 (2021). https://doi.org/10.1021/acssuschemeng.1c00319
7. B. Baral, S. Mansingh, K.H. Reddy, R. Bariki, K. Parida, ACS Omega **5**, 5270 (2020). https://doi.org/10.1021/acsomega.9b04323
8. J. Xu, C. Liu, J. Niu, M. Chen, Sep. Purif. Technol. **230**, 115861 (2020). https://doi.org/10.1016/j.seppur.2019.115861
9. Z. Yu, L. Huang, J. Chen, Y. Tang, B. Xia, D. Tang, Electrochim. Acta **332**, 135473 (2020). https://doi.org/10.1016/j.electacta.2019.135473
10. X. Ren, Q. Wei, F. Wu, Y. Wang, Q. Li, CrystEngComm **23**, 6668 (2021). https://doi.org/10.1039/d1ce00938a
11. L. Pang, Q. Ma, C. Zhu, J. Electron. Mater. **52**, 1808 (2023). https://doi.org/10.1007/s11664-022-10194-9
12. H. Luo, S. Dimitrov, M. Daboczi et al., ACS Appl. Nano Mater. **3**, 3371 (2020). https://doi.org/10.1021/acsanm.9b02412
13. L. Li, B. Yu, T. You, Biosens. Bioelectron. **74**, 263 (2015). https://doi.org/10.1016/j.bios.2015.06.050
14. C. Xie, B. Nie, L. Zeng et al., ACS Nano **8**, 4015 (2014). https://doi.org/10.1021/nn501001j

15. X. Li, M. Rui, J. Song, Z. Shen, H. Zeng, Adv. Funct. Mater. **25**, 4929 (2015). https://doi.org/10.1002/adfm.201501250

16. Y. Yao, Z. Jin, Y. Chen et al., Carbon **129**, 228 (2018). https://doi.org/10.1016/j.carbon.2017.12.024

17. Y. Yao, M. Yin, J. Yan, D. Yang, S. Liu, Sens. Actuators B **251**, 583 (2017). https://doi.org/10.1016/j.snb.2017.05.007

18. T. Selvakumar, M. Rajaram, A. Natarajan, L. Harikrishnan, K. Alwar, A. Rajaram, ACS Omega **7**, 12825 (2022). https://doi.org/10.1021/acsomega.2c00092

19. Y. Li, Y. Hu, Y. Zhao et al., Adv. Mater. **23**, 776 (2011). https://doi.org/10.1002/adma.201003819

20. Y. Zhao, D. Yu, J. Lu et al., Adv. Opt. Mater. **7**, 1901085 (2019). https://doi.org/10.1002/adom.201901085

21. T. Wu, J. Gliniak, J. Lin et al., Chemsuschem **10**, 3260 (2017). https://doi.org/10.1002/cssc.201700910

22. S. Ahirwar, S. Mallick, D. Bahadur, ACS Omega **2**, 8343 (2017). https://doi.org/10.1021/acsomega.7b01539

23. H. Huang, S. Yang, Q. Li et al., Langmuir **34**, 250 (2018). https://doi.org/10.1021/acs.langmuir.7b03425

24. H. Xu, Y. Wang, X. Dong, N. Zheng, H. Ma, X. Zhang, Appl. Catal. B **257**, 117932 (2019). https://doi.org/10.1016/j.apcatb.2019.117932

25. Y. Li, Y. Zhao, H. Cheng et al., J. Am. Chem. Soc. **134**, 15 (2012). https://doi.org/10.1021/ja206030c

26. X.T. Zheng, A. Ananthanarayanan, K.Q. Luo, P. Chen, Small **11**, 1620 (2015). https://doi.org/10.1002/smll.201402648

27. C. Liu, L. Bao, M. Yang et al., J. Phys. Chem. Lett. **10**, 3621 (2019). https://doi.org/10.1021/acs.jpclett.9b01339

28. T. Selvakumar, M. Rajaram, A. Natarajan et al., J. Mater. Sci. Mater. Electron. **34**, 417 (2023). https://doi.org/10.1007/s10854-023-09855-0

29. H. Li, R. Liu, Y. Liu et al., J. Mater. Chem. **22**, 17470 (2012). https://doi.org/10.1039/c2jm32827e

30. J. Zhao, C. Chen, W. Ma, Top. Catal. **35**, 269 (2005). https://doi.org/10.1007/s11244-005-3834-0

31. Z. He, M.S. Siddique, H. Yang et al., J. Clean. Prod. **339**, 130634 (2022). https://doi.org/10.1016/j.jclepro.2022.130634

32. X. Zheng, Y. Fan, H. Peng, J. Wen, Colloids Surf. A **627**, 127126 (2021). https://doi.org/10.1016/j.colsurfa.2021.127126

33. H. Cui, S. Dong, K. Wang, M. Luan, T. Huang, Sep. Purif. Technol. **255**, 117758 (2021). https://doi.org/10.1016/j.seppur.2020.117758

34. R. Vinu, S.U. Akki, G. Madras, J. Haz. Mater. **176**, 765 (2010). https://doi.org/10.1016/j.jhazmat.2009.11.101

35. A. Houas, H. Lachheb, M. Ksibi, E. Elaloui, C. Guillard, J.M. Herrmann, Appl. Catal. B **31**, 145 (2001). https://doi.org/10.1016/S0926-3373(00)00276-9

36. X. Fu, L. Wang, Z. He, Y. Gao, Y. Xia, J. Tao, J. Mater. Sci. Mater. Electron. **34**, 698 (2023). https://doi.org/10.1007/s10854-023-10143-0

37. X. Fu, L. Wang, Z. He et al., J. Solid State Chem. **319**, 123794 (2023). https://doi.org/10.1016/j.jssc.2022.123794

38. Z. Yu, S.S.C. Chuang, J. Phys. Chem. C **111**, 13813 (2007). https://doi.org/10.1021/jp0715474

39. M.A. Rauf, M.A. Meetani, A. Khaleel, A. Ahmed, Chem. Eng. J. **157**, 373 (2010). https://doi.org/10.1016/j.cej.2009.11.017

40. Y. Yao, W. Dong, Z. Zhao, H. Cui, G. Liao, Colloids Surf. A **649**, 129533 (2022). https://doi.org/10.1016/j.colsurfa.2022.129533

41. Y. Yao, G. Liao, H. Cui, W. Dong, Z. Zhao, J. Mater. Sci. Mater. Electron. **34**, 1445 (2023). https://doi.org/10.1007/s10854-023-10870-4

42. T. Rager, A. Geoffroy, R. Hilfiker, J.M. Storey, Phys. Chem. Chem. Phys. **14**, 8074 (2012). https://doi.org/10.1039/c2cp40128b

43. L. Luo, W. Chen, S.M. Xu et al., J. Am. Chem. Soc. **144**, 7720 (2022). https://doi.org/10.1021/jacs.2c00465

44. Y. Yao, F. Ji, M. Yin et al., ACS Appl. Mater. Interfaces **28**, 18165 (2016). https://doi.org/10.1021/acsami.6b04692

45. X. An, J.C. Yu, F. Wang, C. Li, Y. Li, Appl. Catal. B **129**, 80 (2013). https://doi.org/10.1016/j.apcatb.2012.09.008

46. L. Zhang, Z.C. Ding, T. Tong, J. Liu, Nanoscale **9**, 3524 (2017). https://doi.org/10.1039/c7nr00136c

47. X. Cao, Z. Lei, B. Huang et al., Small **18**, e2200445 (2022). https://doi.org/10.1002/smll.202200445

48. R. Miao, Z. Luo, W. Zhong et al., Appl. Catal. B **189**, 26 (2016). https://doi.org/10.1016/j.apcatb.2016.01.070

49. H. Leelavathi, R. Muralidharan, N. Abirami et al., Colloids Surf. A **656**, 130449 (2023). https://doi.org/10.1016/j.colsurfa.2022.130449

50. H. Leelavathi, R. Muralidharan, N. Abirami, New J. Chem. **47**, 7774 (2023). https://doi.org/10.1039/d3nj00660c